# Calculation and interpretation of *K*-shell x-ray absorption near-edge structure of transition metal oxides

H. Modrow and S. Bucher
*Physikalisches Institut, University of Bonn, D-53115 Bonn, Germany*

J. J. Rehr and A. L. Ankudinov
*Department of Physics, University of Washington, Seattle, Washington 98195*

(Received 10 July 2002; published 31 January 2003)

Simultaneous calculations of both *K*-edge x-ray-absorption near-edge structure (XANES) and ground-state electronic structure of 3*d* transition-metal oxides are presented. The calculations are based on a self-consistent one-electron real-space Green's-function approach, with many-body effects incorporated in terms of final-state potentials and a complex energy-dependent self-energy. The results are found to be in semiquantitative agreement with experiment at the metal *K* edges, except at the edge itself where a leading edge peak is found to be systematically low in intensity. A scattering theoretic interpretation is presented, which correlates the structure in the XANES with projected electronic density of states. This interpretation illustrates the crossover from a molecular orbital to a continuum resonance description of excited states. The importance of the core-hole potential in these calculations is also discussed.

DOI: 10.1103/PhysRevB.67.035123 PACS number(s): 78.70.Dm, 33.20.Rm, 71.20.−b

## I. INTRODUCTION

There has been a considerable interest in the use of x-ray-absorption near-edge structure (XANES) spectra to understand aspects of the electronic structure in materials' studies. This includes, for example, oxidation states, charge transfer, and the nature of the low-energy excited states.[1] Transition-metal monoxide (TMO) systems are prototypical of such studies and have been the object of many investigations.[2–4] Due to short, strong chemical bonds with valence $\pm 2$, TMO's often crystallize in the NaCl salt structure. However, the interpretation of the observed XANES in these systems has been controversial. For example, the classic study of Grunes[2] argued that certain features in the *K*-edge spectra could not be interpreted in terms of a one-electron formalism. Also, recent studies of the *L*-edge spectra of these materials suggest that many-electron effects in atomic-multiplet theory are important for an accurate description.[5–10] However, others[4] have argued that one-electron calculations of the *K*-shell spectra appear qualitatively to replicate the main peaks. Our treatment below is based on an effective one-electron theory, based on a self-consistent, real-space Green's-function (RSGF) formalism and final-state potentials including a screened core hole. In particular, the approach uses spherical muffin-tin potentials and many-body effects and inelastic losses are included in terms of an energy-dependent self-energy. This theory is implemented in the *ab initio* XANES and electronic structure code FEFF8.[11] The purpose of this paper is to investigate the validity of this approach, both for calculations and interpretation of the *K*-edge XANES spectra of the TMO's. Indeed, we find that our approach verifies the final-state rule,[12] that the spectra can be calculated with a one-electron theory with final-state potentials. Our treatment of electronic structure is formally equivalent to the Korringa-Kohn-Rostocker band-structure theory, but carried out in real space and in the presence of a core hole which breaks crystal translational symmetry. At the same time, the theory provides a quantitative relation between the projected electronic density of states (*l*DOS) and the absorption spectra, as well as a physical description of the observed XANES. The treatment thus encompasses both the excited state and the multiple-scattering (MS) path descriptions of x-ray-absorption spectra (XAS).

Calculations of XANES differ significantly from those of conventional ground-state electronic structure, since XANES probes low-energy excited states which have a finite lifetime in the presence of a core hole. Thus, the theoretical ingredients are also different. For the ground state, for example, self-consistent band-structure (BS) or the molecular-orbital (MO) techniques of quantum chemistry deal well with occupied stationary states, even at moderate temperature. These methods can also treat excited states approximately, but are generally restricted to low energies, typically less than about 50 eV from threshold due to basis size limitations. Also such methods often include final-state lifetimes *a posteriori* in terms of Lorentzian broadening, but ignore self-energy effects which systematically shift the spectra to higher energies.[13,14] On the other hand, excited states in the continuum tend to be extended and damped, with finite lifetimes (due to core-hole and final-state broadening) that limit their range to about 20 Å or less. Some low-lying band states encountered in the ground state can be well localized and sharply defined in energy, and hence correspond closely to a MO interpretation, whereas highly excited states tend to form broad resonances. The XANES lies in the transition region between these behaviors. The approach used in the FEFF8 code encompasses both regimes by using a continuum MS theory, which can be extended to arbitrarily high energies and naturally includes broadening and lifetime effects in terms of a self-energy. Although, full multiple-scattering (FMS) calculations become computationally prohibitive for extended x-ray-absorption fine structure (EXAFS) (i.e., the fine structure in XAS's above about 50 eV), the MS expansion crosses over to a more rapidly convergent path expan-

 

TABLE I. Electron transfer $\Delta e$ and $l$-projected charge counts for spectator atoms in different (+II) transition-metal oxides. TM symbolizes transition-metal atom, O oxygen, and SG the space group.

| | SG | $\Delta e$ | TM $s$ | TM $p$ | TM $d$ | O $s$ | O $p$ | O $d$ |
|---|---|---|---|---|---|---|---|---|
| CaO | fm3m | −0.397 | 0.303 | 0.443 | 0.855 | 1.855 | 4.518 | 0.024 |
| TiO | fm3m | −0.323 | 0.341 | 0.538 | 2.800 | 1.777 | 4.420 | 0.126 |
| VO | fm3m | −0.286 | 0.352 | 0.567 | 3.796 | 1.757 | 4.406 | 0.124 |
| MnO | fm3m | −0.209 | 0.439 | 0.602 | 5.751 | 1.819 | 4.328 | 0.062 |
| CoO | fm3m | −0.169 | 0.466 | 0.628 | 7.739 | 1.841 | 4.241 | 0.087 |
| NiO | fm3m | −0.162 | 0.476 | 0.641 | 8.723 | 1.845 | 4.225 | 0.092 |
| CuO | c2/c | −0.359 | 0.534 | 0.624 | 9.484 | 1.862 | 4.404 | 0.097 |
| ZnO | p63mc | −0.285 | 0.709 | 0.886 | 10.129 | 1.896 | 4.312 | 0.071 |

sion typically around 20–30 eV above threshold.[13] For the near-edge structure, the FEFF8 code also provides a scattering theoretic interpretation in terms of electronic structure, e.g., the angular momentum projected local density of states, which is complementary to the discrete state or MO interpretation. A path by path interpretation combined with a Fourier transformation of the spectra is traditionally used in EXAFS analysis to interpret the spectra in real space. This works well since electron scattering is relatively weak at high energies, where the MS expansion converges with of order $10^2-10^3$ scattering paths. On the other hand, a discrete state picture is commonly used in XANES, since it has an intuitive chemical interpretation in terms of local electronic states and their splittings. In principle, MS results are equivalent to BS or MO results, provided the calculations are carried to sufficiently high or infinite order.[15] However, poor convergence of the path expansion is often observed near threshold, thereby often necessitating a FMS approach.

The present results contain a number of approximations. For example, the theory used in FEFF8 is essentially a broadened final-state one-electron theory consistent with the final-state rule,[12] i.e., a theory based on self-consistent, final-state potentials, which are essential for a correct reproduction of near-edge features and an accurate value of the threshold or Fermi energy. The scattering potential is approximated by overlapped spherical muffin-tin potentials (including a core hole); overlapping the muffin tins by about 15% compensates partly for the errors in the spherical approximation. Many-body effects are incorporated approximately in terms of a complex, energy-dependent self-energy, which replaces the exchange-correlation potential of ground-state density-functional theory. We have used the Hedin-Lundqvist electron-gas self-energy, within the plasmon-pole approximation, which has been well tested for XAS studies.[13] This self-energy naturally adds important final-state broadening and self-energy shifts, but does not contribute any new features to the spectra.

The content of the remainder of this paper is as follows: A short description of the experimental parameters is given in Sec. II, while Sec. III describes our calculation strategy based on the RSGF formalism in FEFF8.[11] In Sec. IV, we focus on calculations of the $K$-shell XANES for several transition-metal monoxides listed in Table I, and we also give a scattering theoretic interpretation of the spectra. Section V contains a summary and conclusions.

## II. EXPERIMENTAL DETAILS

All x-ray-absorption measurements described here were performed on beamline BN3 of the Electron Stretcher and Accelerator (ELSA) at Bonn University. For the measurements at the $K$ edges of elements with $Z \leqslant 27$, ELSA was operated at an electron energy of 2.3 GeV and an average electron current of 35 mA. Measurements at elements with $Z > 27$ were performed at 2.7 GeV and an average electron current of 25 mA. Monochromatic light was obtained by using a double-crystal monochromator of Lemonnier type,[16] which was equipped with Ge(220) crystals ($2d = 4.0$ Å).[17] The minimum step width of these crystals increases from about 0.12 eV at the Ca $K$ edge (4038.5 eV) to about 1 eV at the Zn $K$ edge (9659 eV). All spectra were taken in transmission mode. Depending on the energy of the edge under investigation and the air sensitivity of the samples, the ionization chambers were filled with either air or argon at different pressures.

Balzers QM311 electrometers were used to read the ionization currents and yield a voltage proportional to the ionization current. These voltages were read using an AD/DA card of type DT2836 by data translation. The photon energy was scanned from at least 40 eV before to 100 eV after the rising edge. For each data point, an integration time between 200 and 400 ms was used. To prepare the samples for measurement, the oxide powders were evenly applied to self-adhesive kapton tape. For air sensitive samples, this process took place in a glove box filled with argon. These samples were transferred to the measurement chamber under argon atmosphere as well. To compare the measurements qualitatively, a linear background—fitted in the pre-edge region—was subtracted and the absorption edge was normalized to unity about 50 eV above the edge. Photon energy calibration at all $K$ edges is made in relation to the pure metal: the first inflection point is set to the binding energy of the $1s$ electron given in Ref. 17.

## III. XANES CALCULATIONS WITH FEFF8

### A. Multiple-scattering formalism

Multiple-scattering XANES calculations are more challenging than EXAFS calculations, since electron scattering is much stronger at low energies, and hence XANES is much more sensitive to details of the scattering potential and to high-order MS paths.[11] Thus a self-consistent field (SCF) potential and nonspherical corrections are essential for the occupied states in ground-state theory and may be important for the low-lying excited states in XANES, but are generally not needed for EXAFS calculations. A review of high-order MS theory and its applications to EXAFS and XANES calculations is given in Ref. 13. Other details concerning the RSGF method and its application to XANES are given in the primary FEFF8 reference.[11]

The MS expansion may converge poorly or even diverge in XANES, due to the increase of the mean free path and backscattering amplitude near threshold. However, these

considerations are system dependent. For close-packed metals and oxides, self-consistency appears to have only a minor effect on the spectra beyond a few eV of the edge, but is essential to obtain the threshold energy and edge shape, and hence charge counts. Even more important are the self-energy and inelastic losses, which lead to systematic shifts and damping of the peaks. Based on the agreement between theory and experiment achieved here, nonspherical corrections do not appear to be significant for TMO's, except very close (i.e., within a few eV) to the edge, where the calculated leading peak intensity is generally smaller than that observed.

Although FEFF8 is not a total-energy code, its potential construction does build in overall charge neutrality. This is done by fixing muffin-tin radii based on the Norman prescription, i.e., they are set to a fixed fraction of the Norman radii (analogous to Wigner-Seitz radii in crystals) which are defined by enforcing charge neutrality in a sphere surrounding a given atom. For the metal monoxides, this prescription gives the metal a volume fraction of 0.65. This value is in good agreement with the self-consistent, total-energy atomic sphere approximation calculations of Andersen[3] for TMO's, which finds that the metal has a volume of about 2/3 a fcc unit cell. Remarkably, this indicates that the FEFF8 prescription is close to that for the lowest total-energy configuration.

Within the MS formalism of RSGF theory, the XANES calculations depend on three main ingredients: (i) the spherical muffin-tin potential, which is contained implicitly in the (dimensionless) diagonal scattering $t$-matrix elements $t_l = \exp(i\delta_l)\sin(\delta_l)$, where $\delta_l$ is the $l$-wave phase shift; (ii) the two center matrix elements of the free propagator $G^0_{L,R;L'R'}(E)$, and (iii) the relativistic dipole matrix elements between core and continuum embedded-atomic states. The muffin-tin potential has a much stronger influence on the XANES spectra than on EXAFS, since it can strongly influence the dipole matrix elements. Some other commonly used electronic structure calculations use rather similar ingredients. For example, the linear muffin-tin orbital approach also uses spherical potentials but a somewhat different self-consistent potential construction and linearized phase shifts.[18] The key differences are the inclusion of a core hole and an energy-dependent self-energy in our approach.

Since details of the FEFF8 approach have been published elsewhere,[11] we only briefly summarize the method here. In the algorithm for the scattering potential, the total electron density is first approximated by overlapped free-atom densities, using a relativistic Dirac-Fock code, with a core hole in the $1s$ level ($K$ shell) of the absorbing atom. Then the scattering potential is calculated by solving Poisson's equation, adding local exchange, and imposing spherical symmetry in muffin-tin form. With the new potential, new densities are calculated, and the potential and density are iterated until self-consistency is reached. This typically requires about ten iterations, using the Broyden algorithm to accelerate convergence.[11] Tests have verified that the ground-state DOS obtained in this procedure with clusters of about 150 atoms are in good agreement with those of full-potential linear augmented plane-wave (LAPW) band-structure calculations in the WIEN98 code.[19] Finally, an energy- and density-dependent self-energy $\Sigma(E)$ is added. Once the SCF scattering potential is determined, the remaining ingredients (phase shifts, matrix elements, etc.) are then calculated. Thus the approach incorporates a self-consistent, screened core-hole potential, in accordance with the final-state rule.

In this method, the photoelectron self-energy $\Sigma(E)$ enters as an energy- and density-dependent contribution to the muffin-tin potential. The self-energy together with the core-hole lifetime builds in both losses [i.e., the mean free path $\lambda \approx k/|\mathrm{Im}\Sigma(E_k)|$] as well as energy-dependent shifts in the peak positions due to $\mathrm{Re}\Sigma(E)$. Debye-Waller factors are small in XANES's, but are incorporated approximately by a multiplicative factor $\exp(-k^2\sigma^2_{R,R'})$ in each propagator matrix element $G^0_{L,R;L'R'}$, where $\sigma^2$ is a temperature-dependent mean-square vibrational amplitude for the bond $(R,R')$. The lifetime broadened Fermi factor is included by a complex energy plane integral, which is more accurate than a Lorentzian convolution.

### B. Need for self-consistency and full MS

It is instructive to compare the results of calculations using different levels of theory in order to assess the importance of the various refinements. Figure 1 demonstrates clearly the importance of the FMS approach and self-consistency, using CaO as an example. The calculations in the top row (a,b) are based on FMS with fewer than 100 atoms in the cluster. The calculations in the bottom row (c,d) are obtained using the high-order path expansion within a cluster of radius 8 Å and include roughly 200 atoms. In both cases, only the calculations on the left panel (a,c) are based on self-consistent potentials. The breakdown of the path expansion close to the absorption edge is easily recognized from the presence of large amplitude structures, which can even yield unphysical negative values (c,d). However, note that the path expansion (c), even without self-consistency (d), is a reasonable approximation beyond about 30 eV of threshold. On the other hand, it is clear that self-consistency is essential for an accurate description of the absorption edge and the relative energy position of the two dominating resonances, i.e., the structure within about 10 eV of threshold, as illustrated in (a).

## IV. RESULTS AND DISCUSSION

### A. Qualitative comparison with experiment

In order to illustrate both the strengths and shortcomings of the theoretical approach used in FEFF8, it is instructive first to consider one example in detail. To this end, we consider the case of Rutile, a modification of $TiO_2$ which has been discussed extensively in literature.[20–23] As shown in Fig. 2, our approach appears to reproduce all significant XANES peaks. However, a notable drawback is that the intensity of the low-energy side of the ''white line'' (i.e., a dominant edge peak) is too low. The underestimation of this leading edge peak is typical throughout the transition-metal (TM) oxides (cf., Fig. 3), whereas otherwise semiquantitative

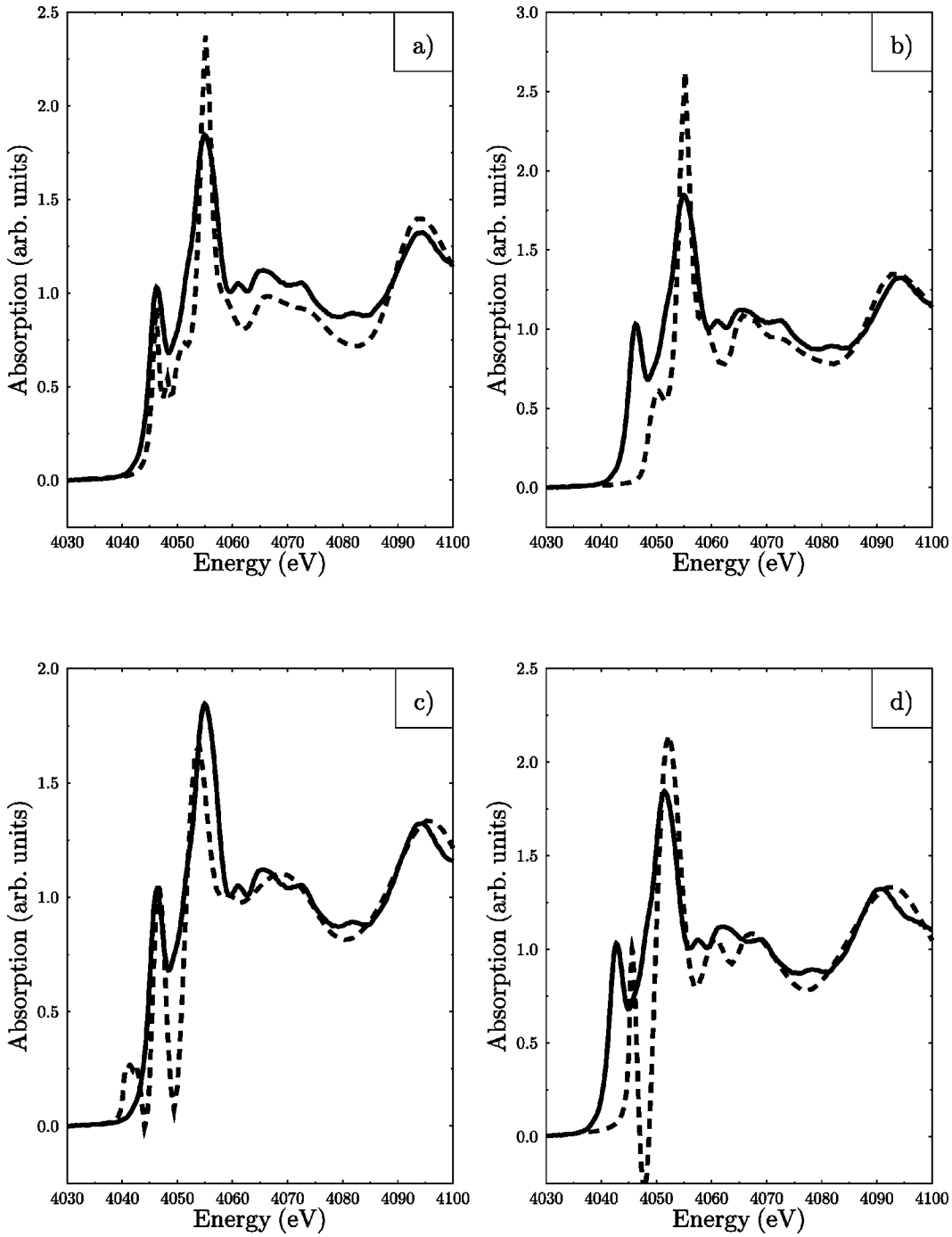


FIG. 1. Calculations (dashed) of the Ca *K*-edge XANES of CaO using (a) SCF and FMS, (b) non-SCF and FMS, (c) SCF and path expansion, (d) non-SCF and path expansion, and compared to experimental data (solid).

agreement with experimental data is always achieved. A comparable discrepancy is not observed for the *K*-edge structure of pure transition metals.

Further analysis suggests that the discrepancy is likely due to nonspherical contributions from directional chemical bonds, e.g., to a *s*-*p* hybridization effect, analogous to that discussed in Ref. 24. To see this, note that a comparison of the residual between calculated and experimental spectra with the oxygen *p* density of states shows clearly that the discrepancy occurs at the energy positions of maxima in the metal *s*DOS and *p*DOS, as shown in Fig. 2. Thus, *s*-*p* hybridization brought about by nonspherical corrections can alter the relative peak heights. This is corroborated by the improved agreement in peak heights in a method that does include nonspherical corrections.[23] Although it is possible that some of the discrepancy is due to our approximation of core-hole effects, we believe this is a secondary effect, since our calculations already include a fully screened core hole.

Our results for the XANES of all the 3*d*-TM monoxides are shown in Fig. 3: (a) for TM(I) oxides and (b) for TM(II)

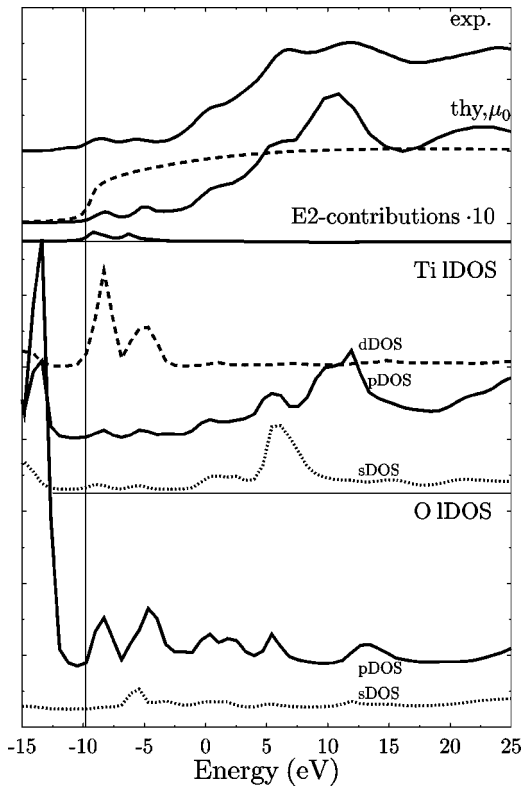


FIG. 2. Experimental data, calculated $\mu$, $\mu_0$, and local *s*, *p*, and *d*-projected density of states at the Ti and O atoms of rutile, respectively. The vertical line indicates the position of the Fermi energy. Also shown is the difference between calculations carried out with and without quadrupolar couplings, which are significantly smaller than the dipole-only contributions in the pre-edge region.

oxides. Our results for the effects of quadrupole coupling in the pre-edge peaks are in reasonable agreement both in amplitude and relative splitting with those of Refs. 21 and 23. Although our calculated quadrupole contributions are both shifted slightly in energy, this shift is likely due to the sensitivity of the quadrupolar contribution to the potentials.[21,23] Our results are illustrated in Fig. 2(a), where we also give the polarization averaged difference between calculations including quadrupole couplings and dipole only. Thus, we find that quadrupole effects are small in comparison with the dipole contributions from *p*-*d* hybridization effects.

### B. Scattering interpretation of XANES

We now turn to a physical interpretation of the spectra. To do this, we compare *K*-shell XAS to the corresponding final state *l*DOS, which are calculated simultaneously by FEFF8. First we note that each peak in the XAS corresponds closely to a peak in the *p*DOS, both in amplitude and position. This is to be expected, given the close connection between the *l*DOS $\rho_{L,R}$ and the XAS $\mu_{L,R}$ from a given core state of initial angular momentum state $(L_0)$. The XAS is given by the Fermi Golden rule

$$\mu_{L,0}=\sum_f |M_{L_0,L}|^2 \delta(E-E_f)=\langle L_0,0|x\hat{\rho}x'|L_0,0\rangle, \quad (1)$$

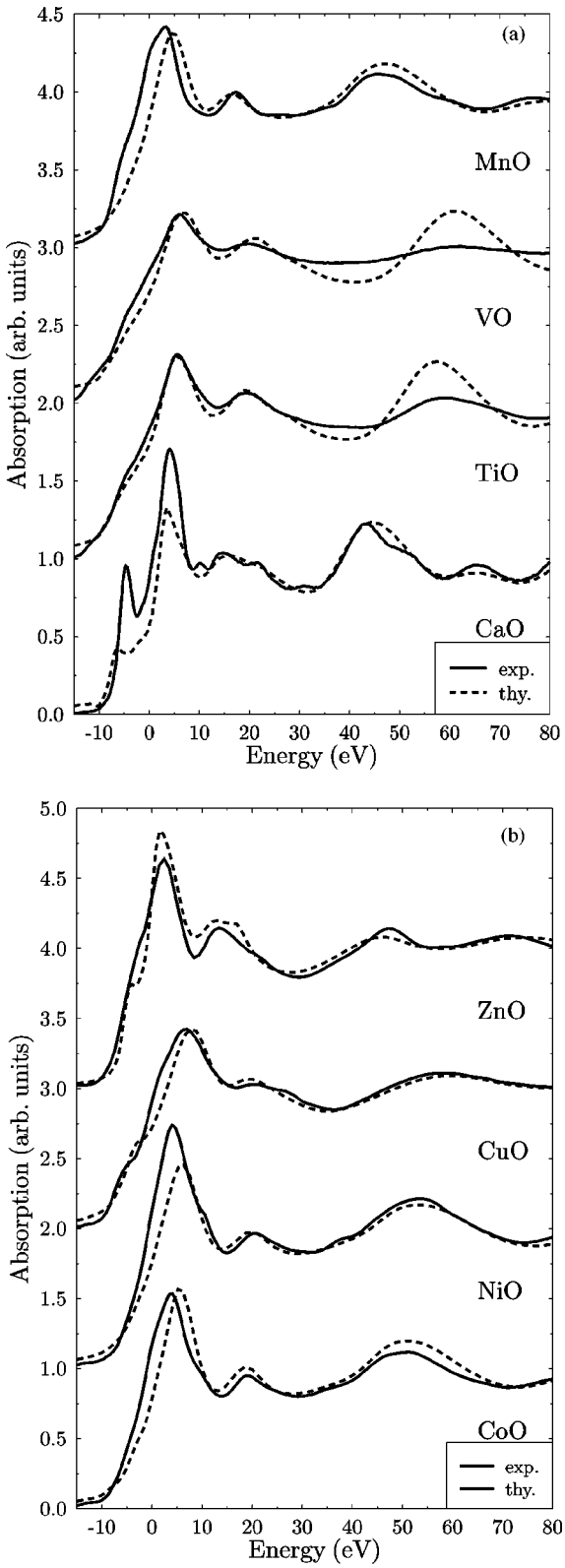


FIG. 3. Experimental (solid) and calculated (dashed) metal *K*-XANES spectra of (a) the transition-metal (I) monoxides MnO, VO, TiO, and CaO, and (b) the transition-metal (II) monoxides ZnO, CuO, NiO, and CoO; additional broadening has been applied to the calculated spectra to account for experimental resolution.

where $M_{L_0,L}=\langle L_0,0|x|f\rangle$ is the dipole matrix element between an initial state of angular momentum $L_0$ and a final state $|f\rangle=|L,0\rangle$ of angular momentum $L$, and $\hat{\rho}=(-1/\pi)\mathrm{Im}G$ is the density matrix, $G$ is the total photoelectron propagator [see Eq. (4) below]. Since they are both matrix elements of the density matrix, $\rho_{l,R}(E)$ and $\mu(E)$ are directly related to each other, and hence due to dipole selection rules, $\mu_{L0}(E)$ directly measures the $l$DOS of the final state $|L,0\rangle$. This relation can be made more quantitative as follows: From MS theory, one can naturally separate the total propagator $G$, and hence $\hat{\rho}$, into a central atom and scattering parts, $G=G^c+G^{sc}$. Thus, the $l$DOS and XAS both have similar XAFS:

$$\rho_{L,R}(E)=\rho^0_{L,R}(E)[1+\chi_{L,R}(E)],$$

$$\mu_{L,R}(E)=\mu^0_{L,R}(E)[1+\chi_{L,R}(E)], \tag{2}$$

and hence,

$$\rho_{L,R}(E)=\gamma(E)\mu_{L,R}(E), \tag{3}$$

where $\gamma(E)=[\rho^0_{L,R}(E)/\mu^0_{L,R}(E)]$.[25] This relation implicitly assumes that the core-hole effect on the spectra is small, which is often a good approximation. More generally, $\rho_{L,R}(E)$ in Eq. (3) refers to the density of states in the presence of a screened core hole. It is important to stress that this relation is also true in cases where previous studies assigned structures in the spectrum to $1s\rightarrow 3d$ transitions, i.e., quadrupole transitions. However, true quadrupole transitions are very small; they are suppressed by a factor approximately $(r_{1s}/\lambda)^2$, where $\lambda$ is the wavelength of the photon and $r_{1s}\sim 1/Z$ is the mean radius of the $1s$ orbital, i.e., by a factor of order $\leqslant 10^{-2}$. The quadrupolelike effect that is observed is actually band hybridization, which mixes $p$-type states into the $d$ bands and, consequently, gives a dipole allowed transition. This fact shows clearly, e.g., when analyzing the ''pre-edge structure'' in the rutile $l$DOS (see Fig. 2). Note that the double structure in the transition-metal $p$DOS at the low-energy part of the absorption edge does *not* coincide with the maxima of the $d$DOS as it should, if we were facing a dominant contribution of a quadrupole transition. Only a very weak edge peak in the experimental spectrum just below the double peak has been associated with a pure quadrupole transition.[23] Moreover, the energy positions of all significant experimental XANES peaks coincide with those calculated with only dipole selection rules, without regard for excitonic or shake-up structures. Therefore, it can be concluded that such effects are essentially negligible for the interpretation of $K$-shell absorption spectra of the TMO's.

### C. MO Interpretation of XANES

Next, we investigate to what extent MO theory is applicable to the analysis of the various XANES, following the treatment of Grunes.[2] For this analysis, we will use CoO as a typical example; results for the other TMO's are similar.

The FEFF8 code is based on a Green's-function formalism in the complex energy plane, which avoids explicit calculations of wave functions or molecular orbitals. However, a connection between the Green's-function function and the wave-function approach can be made using the formal spectral decomposition of the Green's-function operator $G$ in terms of eigenstates $|f\rangle$, viz,

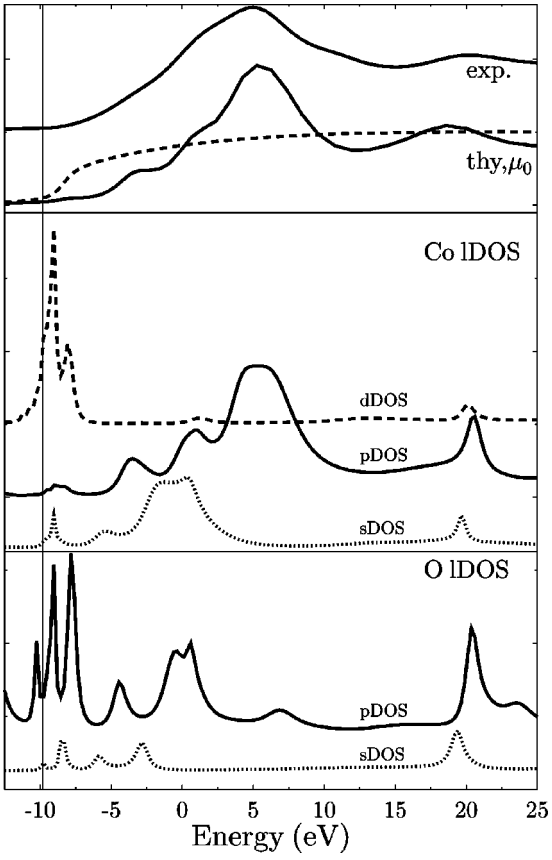


FIG. 4. Relations between experimental data, calculated $\mu$, $\mu_0$, and $l$-projected density of valence states at the Co and O atoms of CoO, respectively. The vertical line indicates the position of the Fermi energy.

$$G=(E-H)^{-1}=\sum_f |f\rangle\frac{1}{E-E_f+i\Gamma}\langle f|, \tag{4}$$

and similarly for the density matrix $\hat{\rho}=-(1/\pi)\mathrm{Im}G$. Our electronic structure interpretation of XANES makes use of the angular momentum projected density of states $\rho_{l,R}(E)$ at a given site $R$,

$$\rho_{l,R}(E)=\langle L,R|\hat{\rho}|L,R\rangle=\sum_f |c_{L,R}|^2\delta(E-E_f), \tag{5}$$

where $|c_{L,R}|^2=|\langle L,R|f\rangle|^2$ represents the probability of the final state to be in the local state $|L,R\rangle$, where $L=(l,m)$ denotes the angular momentum quantum numbers. Thus, peaks in the $l$DOS correspond roughly to the energy eigenvalues of a MO approach.

Figure 4 shows the experimental spectrum of CoO together with the XAS and $l$DOS calculated by FEFF8. The good overall agreement between calculated and measured spectra is notable. As in the case of rutile above, we suggest

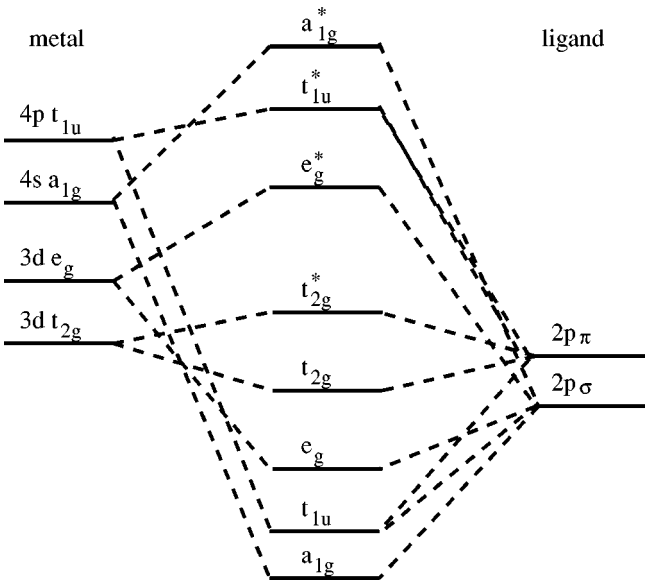


FIG. 5. Schematic display of the ligand-field splitting of molecular orbitals in octahedral symmetry.

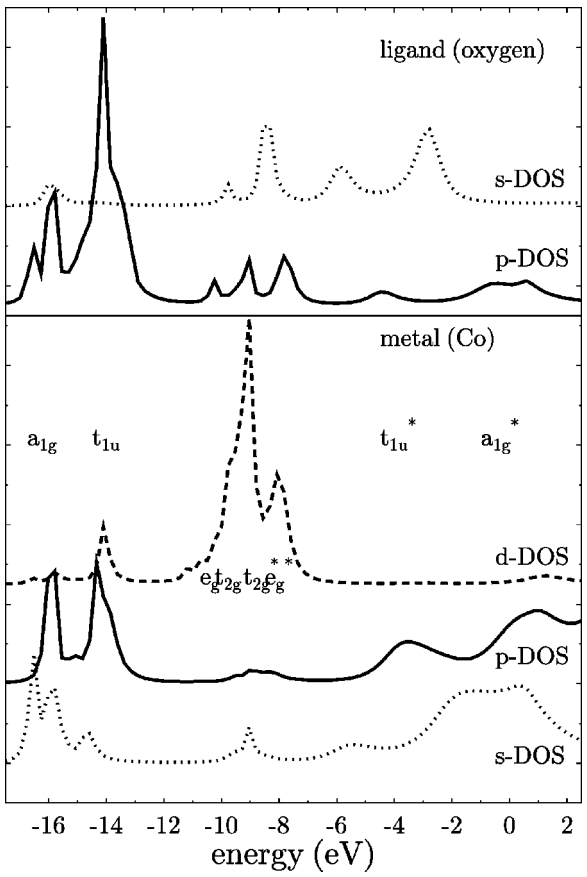


FIG. 6. Analysis of the calculated *l*DOS of CoO in terms of MO theory.

that hybridization with oxygen *p*DOS may explain the observed weakness of the shoulder of the main edge peak at the Fermi level. Let us now focus on the structure in the *l*DOS. Here one can distinguish three regions:

(i) Below and near the Fermi energy, strong, sharp resonances which correspond to quasibound band states dominate the *l*DOS. One can interpret these structures, for example, using the arguments of ligand symmetry MO theory in octahedral symmetry (cf. Figs. 5 and 6). As bonding molecular orbitals, one expects one of $a_{1g}$ symmetry, which is easily identified by contributions of the metal 4*s* orbital, a threefold degenerate $t_{1u}$ orbital, to which metal 4*p* orbitals should contribute, and a twofold degenerate $e_g$ orbital, which can be recognized by its strong metal 3*d* contributions. Next comes the essentially nonbonding $t_{2g}$ orbital (the formation of $\pi$ bonds from the ligand to these orbitals is possible and indicated by the presence of *p*DOS at the oxygen atom in this energy range), formed by the remaining metal 3*d* orbitals, followed by the $e_g^*$ orbital. MO theory, by its nature, does not take into account any band-structure effects, which lead to a ''contamination'' of the pure MO peaks by band hybridization. An example of this effect is the presence of metal *s*DOS in the energy range of the $t_{1u}$ orbital, which cannot be present from a pure MO point of view.

(ii) MO theory expects two more orbitals of symmetry $a_{1g}^*$ and $t_{1u}^*$, determined mainly by metal 4s and metal 4*p* orbitals, respectively. These structures can also be located in the *l*DOS obtained by our calculations in the region between Fermi energy and vacuum level, as shown in Fig. 6. They are, however, of a completely different shape. Their broadening reflects the fact that these final states have a finite lifetime due to their nature as excited states. Furthermore, they are shifted energywise, both because of the energy-dependent complex self-energy.

(iii) Above the vacuum energy, one expects a smooth background with some sharp resonances. For the analysis of the spectrum in the region above $E_{vac}$, MO theory is not always directly applicable, although hybridization effects as discussed in Ref. 24 are still possible. Thus, the attribution of the white line in the TMO's to a $1s \rightarrow 4p$ transition, which often used in the literature, is strictly only a rough approximation. Also, the quasiatomic approach of assigning Rydberg-type states to the resonances fails; neither the intensity of the resonances—after all, one would expect a decreasing overlap integral—nor their energy position is described correctly.

### D. Charge transfer

The output of the FEFF8 code also contains detailed information regarding charge transfer and the local, *l*-projected valence charge.[25] The results, which are summarized in Table I and Fig. 7, can be used directly to analyze the varying influence of the oxygen environment on the electronic structure of different transition-metal atoms. At first, we restrict our considerations to the transition-metal monoxides which have NaCl structure, i.e., the series involving the transition metals Ca to Ni. Due to their octahedral symmetry, a $sp_3d_2$ hybridization is expected. This is reflected by the reduction of *s* charge and corresponding increase of *p* and *d* charge at the TM atoms, compared to their atomic configurations (cf. Table I). In the following discussion, the increase of charge counts relative to the atomic configurations will be referred to as ''surplus charge.'' With increasing occupation of the 3*d*

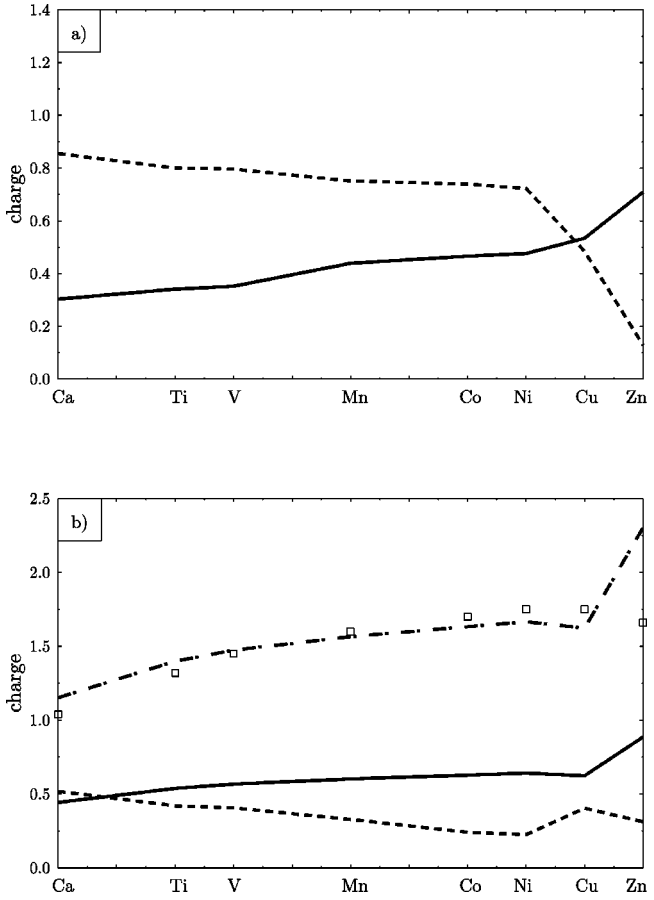


FIG. 7. (a) Calculated occupation numbers for TM *s*-valence (solid line) and surplus TM *d*-valence states (broken line). (b) Calculated occupation numbers for TM *p*-valence (solid line) and surplus Oxygen *p*-(broken line) valence states. To visualize the good agreement between Allred-Rochow electronegativity scale (squares) and TM *p* occupation numbers, rescaled TM *p*-charge counts are also shown (dot and dash).

shell in the atomic configuration, the transfer of the TM *s* charge decreases. This decrease does not affect *p*-shell and *d*-shell occupation equally. Rather, the reduction of metal *s*-charge hybridization is almost equal to the decrease in surplus *d*-charge counts [see Fig. 7(a)]. This effect can be related to increasing repulsive electron-electron interaction due to the increasing occupancy of the *d* states throughout the 3*d* metals. As the changes in *s*- and *d*-charge counts essentially cancel each other, the differences in charge transfer mainly affect *p*-charge counts. This observation can be attributed to the fact that charge transfer occurs mainly from the outermost orbitals, which in the hybridized self-consistent muffin-tin configuration should be metal 4*p* states as well as the strong coupling between metal *s* and ligand *p* states predicted by group theory. The increase of charge in these states contained throughout the series of 3*d* transition metals stems from the growing electronegativity of these elements [see Fig. 7(b)]. In fact, the increase in surplus metal *p* charge throughout the series of 3*d* transition metals correlates well with the Allred-Rochow[26] values for the electronegativity of the corresponding metal within the TMO's belonging to the fm3m space group. Basically, this is to be expected, because in the given configuration of the potential the radially symmetric effective Coulomb interaction approach on which this electronegativity scale is based is exactly reproduced. On the other hand, it should be stressed that charge transfer and thus chemical shift is strongly influenced by geometrical aspects. This fact becomes clear when comparing the charge transfer for CuO and CaO. In CuO, charge transfer increases considerably, almost back to the level observed for CaO in spite of the fact that the electronegativity value for Ca as compared to Cu is smaller by 0.71 (Allred-Rochow) and 0.9 (Pauling), respectively. The charge removed from the TM *p* states is, as one would expect, mainly transferred to oxygen *p* states, as indicated by the high similarity of the curves for oxygen *p* surplus charge and the total charge transfer.

### E. Core-hole effects on XANES

One of the major difficulties in XANES calculations is an adequate description of the core hole. For deep-core *K*-shell XANES, the core-hole photoelectron interaction is relatively weak, and one-electron calculations based on the final-state rule[12] are usually adequate. Thus, we focus here on one-electron effects of the core-hole.

It is interesting to examine how the core-hole effect changes across the TMO series. The presence of the core hole generally leads to a relaxation of all states, lowering their energy eigenvalues. In extended systems, the overlap between the valence orbitals of the absorber atom and surrounding atoms often forms chemical bonds. Hence, relaxation of the valence orbitals can reduce the overlap, weakening a chemical bond. Once the valence orbitals are stabilized, relaxation of the other (virtual) orbitals is also suppressed due to orbital-orbital interaction. This effect is visible in the right panel of Figs. 8(b,d,f), where the *d*DOS calculated with and without the core hole are compared for CaO, MnO, and ZnO, respectively. From CaO to MnO, an increasing number of binding molecular orbitals are occupied. Therefore, stabilization against relaxation of the valence orbitals increases, leading to a strongly reduced core-hole effect for MnO. Continuing throughout the row of 3*d* TMO's, an increasing number of antibinding states is occupied as well, the stabilizing binding energy is reduced, and consequently the core-hole effect gains importance. In the case of ZnO, the core hole influences a closed, noninteracting subshell, which leads to the biggest shift in the energy position of these states. Similar trends are observed when looking at the variations of the core-hole effect on the TM *p*DOS displayed in the left panel of Fig. 8. This is closely correlated to the fact that a strong coupling between metal and ligand *p*-valence states exists, as discussed in the preceding section. Apart from the variation in importance of the core-hole effect seen in Fig. 8, core-hole effects may be partially suppressed by screening. A first approximation, which might be used to describe the two extreme cases, would be to approximate the screening for a ionic insulator as zero and for a conductor as complete. To test this approximation, it is necessary to select materials which have a significant core-hole effect, i.e., whose *l*DOS is strongly influenced by the core hole. Within the series of the

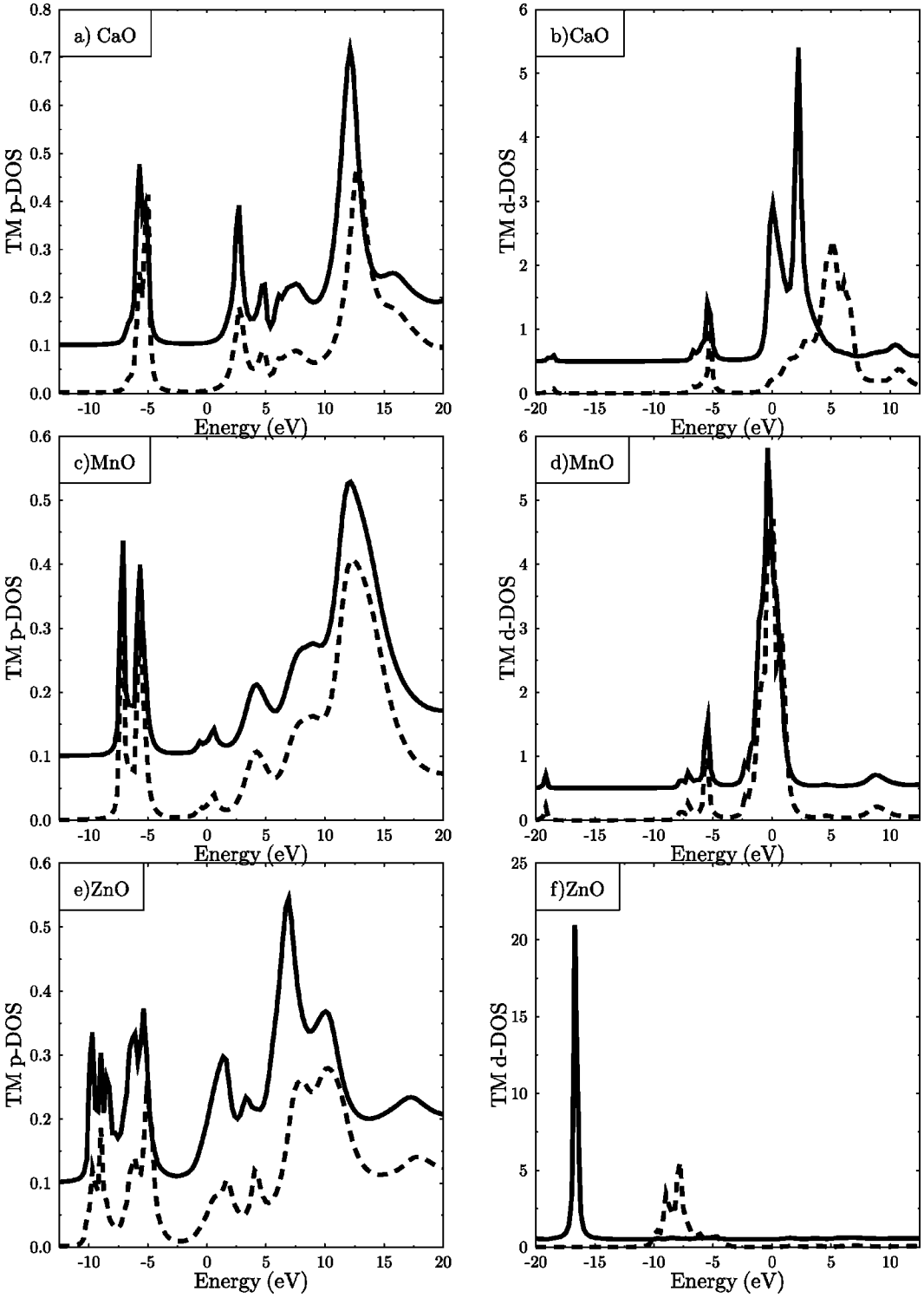


FIG. 8. Comparison between *p*DOS (left panel) and *d*DOS (right panel) of absorber and spectator metal atom for CaO, MnO, and ZnO.

TM(II) oxides, the ionic insulator CaO and the conductor TiO are suitable candidates. Indeed, the CaO spectrum at the Ca *K* edge is clearly dominated by the DOS obtained in the calculation including the core hole. The fact that the Ti *K* spectrum of TiO is dominated by the *l*DOS for the ground state is slightly less evident, but still follows from a careful analysis, e.g., by comparison of the difference in energy between the white line and the first shape resonance of experimental data on the one hand and the *p*DOS obtained with and without a core hole, respectively, on the other. In particular, one observes significant influence of the core hole only for insulators or semiconductors in those cases where the position of valence orbitals is not stabilized by chemical bonding.

## V. CONCLUSIONS

The broadened final-state one-electron calculations presented here are based on the RSGF formalism implemented in the FEFF8 code. These calculations semiquantitatively reproduce almost all features of the transition-metal oxide XANES spectra at the metal *K* edges. To achieve this agreement, both FMS and the use of a self-consistent potential are necessary, especially for energies less than 10 eV above an edge. The good agreement between experiment and our calculations for nanoscale clusters of about 100 atoms demonstrates the adequacy of the approximations used in FEFF8. Thus, an effective one-electron picture is generally sufficient for the TMO *K*-edge XANES, provided an appropriate final-state potential including inelastic losses (in terms of an energy-dependent self-energy) and a screened core hole is used. No evidence for multiplet-electron or sharp multielectron features in the spectra due to many-body effects has been found in our study of *K*-edge spectra. However, the calculated amplitude of a leading white-line peak is found to be somewhat lower than in experiment. The missing intensity is correlated with a peak in the *s*DOS, which suggests that this discrepancy is likely due to directional chemical bonding between the metal and oxygen atoms, and hence is a *s*-*p* hybridization effect. Errors in our treatment of the core hole can also influence the amplitude, but we have argued that they are of secondary importance. Indeed, the general adequacy of our treatment of the core hole for TMO's in terms of fully relaxed final-state potentials has been demonstrated, and is consistent with the final-state rule.[12]

## ACKNOWLEDGMENTS

The authors thank F. de Groot, Ch. Brouder, and F. Farges for useful comments. This work was supported in part by DOE Grant No. DE-FG03-97ER45623 (J.J.R.) and was facilitated by the DOE CMSN.

[1] *X-ray Absorption: Principles, Applications, Techniques of EXAFS, SEXAFS, and XANES*, edited by D.C. Koningsberger and R. Prins (J Wiley, New York, 1988).
[2] L.A. Grunes, Phys. Rev. B **27**, 2111 (1983).
[3] O.K. Andersen, H.L. Skriver, and H. Nohl, Pure Appl. Chem. **52**, 93 (1979).
[4] D. Norman, K.B. Garg, and P.J. Durham, Solid State Commun. **56**, 895 (1985).
[5] Z. Hu, H. Von Lips, M.S. Golden, J. Fink, G. Kaindl, F.M.F. De Groot, S. Ebbinghaus, and A. Reller, Phys. Rev. B **61**, 5262 (2000).
[6] K. Okada and A. Kotani, J. Electron Spectrosc. Relat. Phenom. **62**, 131 (1993).
[7] C. Theil, J. van Elp, and F. Folkman, Phys. Rev. B **59**, 7931 (1999).
[8] M. Abbate, H. Pen, M.T. Czyzyk, F.M.F. de Groot, J.C. Fuggle, Y.J. Ma, C.T. Chen, F. Sette, A. Fujimori, Y. Ueda, and K. Kosuge, J. Electron Spectrosc. Relat. Phenom. **62**, 185 (1993).
[9] A. Kotani and H. Ogasawara, J. Electron Spectrosc. Relat. Phenom. **86**, 65 (1997).
[10] J.C. Parlebas, M.A. Khan, T. Uozumi, K. Okada, and A. Kotani, J. Electron Spectrosc. Relat. Phenom. **71**, 117 (1995).
[11] A. Ankudinov, B. Ravel, J.J. Rehr, and S. Conradson, Phys. Rev. B **58**, 7565 (1998).
[12] U. Von Barth and G. Grossman, Solid State Commun. **32**, 645 (1979).
[13] J.J. Rehr and R.C. Albers, Rev. Mod. Phys. **72**, 621 (2000).
[14] J.E. Müller and J W. Wilkins, Phys. Rev. B **29**, 4331 (1984).
[15] W.L. Schaich, Phys. Rev. B **8**, 4028 (1973).
[16] M. Lemonnier, O. Collet, C. Depautex, J.M. Esteva, and D. Raoux, Nucl. Instrum. Methods **152**, 109 (1978).
[17] *X-Ray Data Booklet*, edited by D. Vaughan (Lawrence Berkeley Laboratory, University of California, Berkeley, 1986).
[18] O.K. Andersen, Phys. Rev. B **12**, 3060 (1975).
[19] P. Blaha, K. Schwarz, P. Sorantin, and S.B. Trickey, Comput. Phys. Commun. **59**, 399 (1990).
[20] R. Brydson, H. Sauer, W. Engel, J.M. Thomas, E. Zeitler, N. Kosugi, and H. Kuroda, J. Phys.: Condens. Matter **1**, 797 (1989).
[21] T. Uozumi, K. Okada, A. Kotani, O. Durmeyer, J.P. Kappler, E. Beaurepaire, and J.C. Parlebas, Europhys. Lett. **18**, 85 (1992).
[22] Z.Y. Wu, G. Ouvrard, P. Gressier, and C.R. Natoli, Phys. Rev. B **55**, 10 382 (1997).
[23] Y. Joly, D. Cabaret, H. Renevier, and C.R. Natoli, Phys. Rev. Lett. **82**, 2398 (1999).
[24] A. Ankudinov, J.J. Rehr, and S.R. Bare, Chem. Phys. Lett. **316**, 495 (2000).
[25] A.I. Nesvizhskii, A.L. Ankudinov, and J.J. Rehr, Phys. Rev. B **63**, 094412 (2000).
[26] A.L. Allred and E.G. Rochow, J. Eng. Power **5**, 264 (1958).